



Quadruple space-group ambiguity owing to rotational and translational noncrystallographic symmetry in human liver fructose-1,6-bisphosphatase

Armin Ruf, Tim Tetaz, Brigitte Schott, Catherine Joseph and Markus G. Rudolph*

Received 3 August 2016
Accepted 18 October 2016

pRED, Therapeutic Modalities, F. Hoffmann-La Roche, 4070 Basel, Switzerland. *Correspondence e-mail: markus.rudolph@roche.com

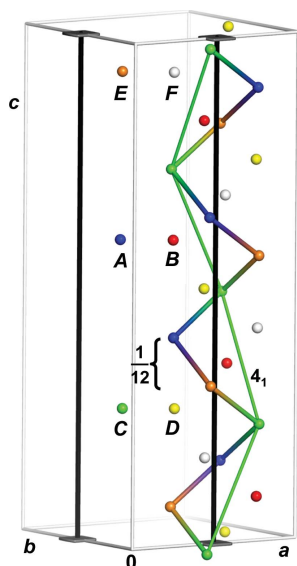
Edited by R. J. Read, University of Cambridge, England

Keywords: pseudo-symmetry; fructose-1,6-bisphosphatase; allosteric regulation; conformational change; glucose metabolism.

PDB reference: human liver FBPase, 5ldz

Supporting information: this article has supporting information at journals.iucr.org/d

Fructose-1,6-bisphosphatase (FBPase) is a key regulator of gluconeogenesis and a potential drug target for type 2 diabetes. FBPase is a homotetramer of 222 symmetry with a major and a minor dimer interface. The dimers connected *via* the minor interface can rotate with respect to each other, leading to the inactive T-state and active R-state conformations of FBPase. Here, the first crystal structure of human liver FBPase in the R-state conformation is presented, determined at a resolution of 2.2 Å in a tetragonal setting that exhibits an unusual arrangement of noncrystallographic symmetry (NCS) elements. Self-Patterson function analysis and various intensity statistics revealed the presence of pseudo-translation and the absence of twinning. The space group is $P4_12_12$, but structure determination was also possible in space groups $P4_32_12$, $P4_122$ and $P4_322$. All solutions have the same arrangement of three C_2 -symmetric dimers spaced by $1/3$ along an NCS axis parallel to the c axis located at $(1/4, 1/4, z)$, which is therefore invisible in a self-rotation function analysis. The solutions in the four space groups are related to one another and emulate a body-centred lattice. If all NCS elements were crystallographic, the space group would be $I4_122$ with a c axis three times shorter and a single FBPase subunit in the asymmetric unit. $I4_122$ is a minimal, non-isomorphic supergroup of the four primitive tetragonal space groups, explaining the space-group ambiguity for this crystal.



1. Introduction

Glucose is the main energy source for the brain. In mammals, blood glucose homeostasis is maintained mainly by the balance of catabolic glycolysis on the one hand and (with respect to glucose) anabolic glycogenolysis and gluconeogenesis on the other. Increased glucose production is the predominant cause of high blood glucose levels in type 2 diabetes, which can lead to kidney, neurological and cardiovascular damage. In humans, high glucose levels arise from excessive gluconeogenesis in the liver rather than from glycogenolysis of hepatic glycogen stores. Fructose 1,6-bisphosphatase (FBPase) is a major control point in gluconeogenesis, catalyzing the hydrolysis of fructose 1,6-bisphosphate (F-1,6-P₂) to fructose 6-phosphate (F6P) and inorganic phosphate (Fig. 1a). This step in gluconeogenesis is synergistically down-regulated by fructose 2,6-bisphosphate (F-2,6-P₂) and AMP, which bind to the active site and an allosteric site of FBPase, respectively. While the cellular level of AMP seems to be constant (Xue *et al.*, 1994), the concentration of F-2,6-P₂ is controlled by the glucagon-sensitive enzyme 6-phosphofructo-2-kinase/fructose-2,6-bisphosphatase.

A small change in the F-2,6-P₂ concentration thus has a large effect on AMP-mediated FBPase inhibition. During times of glucose demand, F-2,6-P₂ levels are reduced, leading to increased activity of FBPase. An aberrant up-regulation of gluconeogenesis, especially when coupled with decreased uptake and metabolism of glucose from the blood into cells, may lead to type 2 diabetes (Visinoni *et al.*, 2012). Inhibition of the liver isoform of FBPase (hFBPase; the other isoform being the muscle isoform) is therefore an attractive avenue for disease treatment.

FBPases are homotetramers with D_2 symmetry composed of 37 kDa subunits. Each subunit contains one active and one allosteric site (Fig. 1*b*). The subunits are labelled C1–C4 and form two functional dimers: C1/C2 and C3/C4. The active site of the C1 subunit is near the C1/C2 interface, while its AMP-binding site is near the C1/C4 interface. The C1/C2 and C3/C4 dimers can rotate with respect to each other. In the enzymatically active R state of the hFBPase tetramer, the dimers are little, if at all, rotated and the protomers are therefore arranged as an almost planar rectangle. In this conformation, a loop important for catalysis (residues 50–72, also termed the

‘dynamic loop’) may either be disordered or folds onto the active site, allowing F-1,6-P₂ to be hydrolyzed (Choe *et al.*, 1998). The hydrolysis reaction requires the presence of Mg²⁺ or Zn²⁺ ions. In contrast, binding of the allosteric regulator AMP facilitates rotation of the dimers by ~15°, leading to detachment of the catalytic loop (Choe *et al.*, 1998). This T state of FBPase is the catalytically inactive conformation.

Structural information on FBPases is available for porcine (no isoforms), rabbit, human liver and human muscle FBPases in the T state (Ke, Zhang *et al.*, 1990; Gidh-Jain *et al.*, 1994; Iversen *et al.*, 1997; Barciszewski *et al.*, 2016) and for porcine and human muscle FBPase in the R state (Ke *et al.*, 1989; Ke, Zhang *et al.*, 1990; Ke, Liang *et al.*, 1991; Ke, Zhang *et al.*, 1991; Choe *et al.*, 1998, 2000; Xue *et al.*, 1994; Weeks *et al.*, 1999; Barciszewski *et al.*, 2016). Crystal structures of porcine FBPase in complex with various ligands established that the R and T states differ from each other by an ~15° rotation of the dimers about the principal molecular axis (Ke, Zhang *et al.*, 1990; Choe *et al.*, 1998). Pushing the FBPase conformational equilibrium towards the inactive T state by allosteric inhibitors that mimic AMP is a well explored route for glucose-level modulation in the blood (Wright *et al.*, 2003; von Geldern *et al.*, 2006; Dang *et al.*, 2007, 2008, 2011; Erion *et al.*, 2005, 2007; Lai *et al.*, 2006; Kitas *et al.*, 2010; Hebeisen *et al.*, 2011; Tsukada *et al.*, 2009, 2010). AMP-site inhibitors connected by a suitable linker to simultaneously bind the AMP sites from two adjacent subunits in the FBPase tetramer gain 10⁵ times in potency compared with monomeric inhibitors (Hebeisen *et al.*, 2008). In addition, a second allosteric site at the C1/C4 interface that is also close to the C1/C2 interface, and hence common to all subunits, has been exploited for inhibitor design (Wright *et al.*, 2002; Choe, Nelson *et al.*, 2003).

For human liver FBPase, currently only T-state structures have been published. Here, we have determined the structure of hFBPase in a novel primitive tetragonal crystal form in the active R state. An interesting combination of rotational NCS (rNCS) and translational NCS (tNCS) allows structure determination in four different space groups comprising two enantiogenic pairs. The combination of a twofold rNCS at a special position with tNCS of vulgar fractions of a unit-cell length leads to pseudo-body-centred tetragonal symmetry, but the true space group is $P4_12_12$. Here, we describe how the rNCS and tNCS emulate pseudo-symmetry and discuss the quaternary

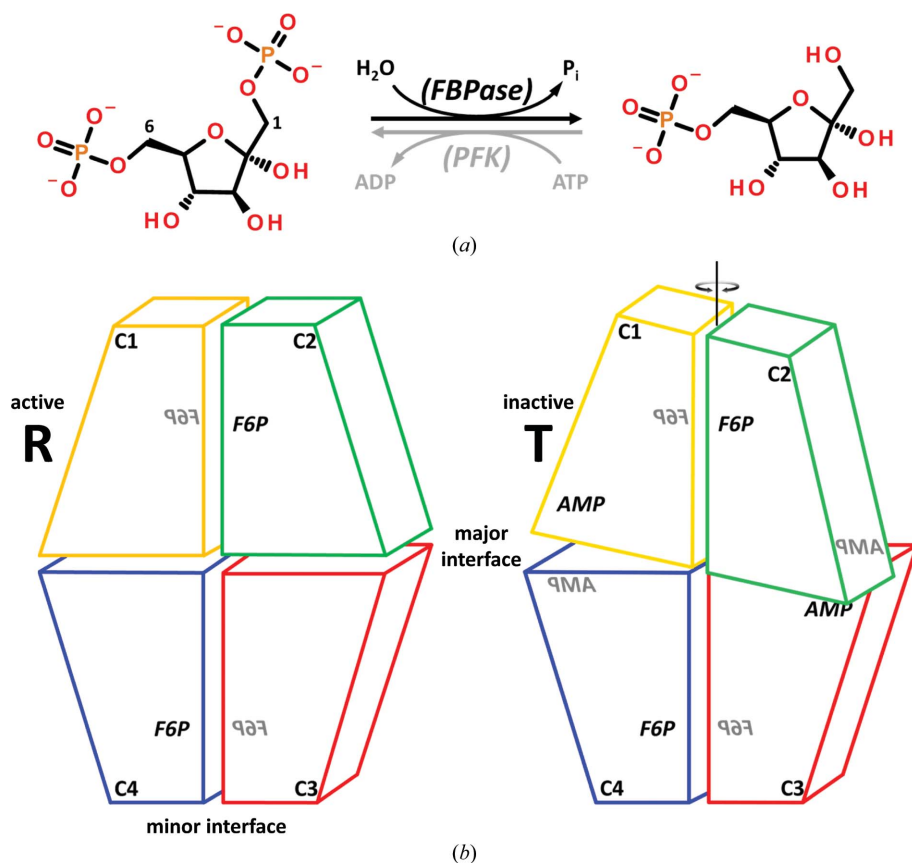


Figure 1

Catalysis and conformational changes of hFBPase. (a) Hydrolysis of fructose 1,6-bisphosphate to fructose 6-phosphate (F6P) by FBPase. The reverse reaction is catalyzed by phosphofructokinase (PFK) at the expense of ATP. (b) Schematic view of the FBPase tetramer and the conformational switch from the active R state (no AMP bound) to the inactive T state (AMP bound). The protomers are labelled C1–C4, with C1/C2 and C3/C4 constituting the functional units that rotate with respect to each other. The active sites for hydrolysis are close to the minor interfaces of these dimers (labelled F6P with the dynamic loop nearby) and the allosteric AMP-binding sites are close to the major interfaces (labelled AMP in the right-hand panel).

Table 1

Data-collection statistics for human liver FBPase.

Resolution range [†] (Å)	39.8–2.2 (2.3–2.2)
100% criterion [‡] (Å)	2.2
Patterson symmetry	<i>P4/mmm</i>
Unit-cell parameters (Å)	<i>a</i> = 121.5, <i>c</i> = 316.6
Total reflections	910459 (51884)
Unique reflections	121210 (11693)
Multiplicity	7.5 (4.4)
Completeness (%)	99.7 (97.9)
<i>R</i> _{merge} [§]	0.132 (1.22)
<i>R</i> _{meas} [§]	0.142 (1.47)
CC _{1/2} [§]	0.997 (0.807)
CC* [§]	0.999 (0.945)
Average <i>I</i> / σ (<i>I</i>)	7.0 (1.1)
Wilson <i>B</i> value (Å ²)	37.3
Mean $ E^2 - 1 $ [¶]	1.152 (0.736/0.541)
$\langle I^2 \rangle / \langle I \rangle^2$	4.224 (2.0/1.5)
$\langle F \rangle^2 / \langle F^2 \rangle$	0.556 (0.785/0.541)
Mean $ L $	0.478 (0.5/0.375)
Mean <i>L</i> ²	0.31 (0.333/0.200)

[†] With the exception of *E* values, moments and *L* values, values in parentheses are for the highest resolution shell. [‡] The 100% criterion was calculated using *SFTOOLS* from *CCP4* (Winn *et al.*, 2011) and represents the resolution in Å of a 100% complete hypothetical data set with the same number of reflections as the measured data. [§] *R* values and CC_{1/2} are defined in Diederichs & Karplus (1997) and Karplus & Diederichs (2012), respectively, and were calculated with *PHENIX* (Zwart, Afonine *et al.*, 2008). *R*_{merge} for the low-resolution shell (39.8–6.1 Å) is 6.0%, indicating that *P422* is the correct symmetry. [¶] *E* values, moments and *L* values are calculated using *PHENIX* (Zwart, Afonine *et al.*, 2008) for acentric reflections in the resolution range 10–3.5 Å. Values in parentheses are the expected values for untwinned and perfectly twinned data, respectively.

structure of hFBPase in light of the R/T transitions in the pig and human FBPase enzymes.

2. Materials and methods

2.1. Protein purification, crystallization and data collection

Human liver FBPase 1 cDNA (NM_000507) was purchased from Origene, cloned into pET-21a *via* the EcoRI/NdeI sites and produced in *Escherichia coli* BL21 (DE3). Cells were suspended in 20 mM Tris–HCl pH 7.5, 1 mM EDTA, 1 mM DTT and disintegrated using a French press. The soluble extract was heated to 65°C for 5 min. The supernatant after centrifugation was applied onto a Macro-Prep High Q column (Bio-Rad) equilibrated in the above buffer. The flowthrough containing FBPase activity was applied onto a Macro-Prep High S column (Bio-Rad) equilibrated with 20 mM HEPES–NaOH pH 7.2, 1 mM DTT. hFBPase was eluted with an NaCl gradient and fractions containing active FBPase were pooled. Size-exclusion chromatography on Sephacryl S200 equilibrated in 20 mM Tris–HCl pH 7.5, 150 mM NaCl, 1 mM EDTA, 1 mM DTT completed the purification. For optimal activity in enzymatic reactions, hFBPase was dialyzed against 10 mM potassium/sodium phosphate pH 7.4, 2 mM MnCl₂, 5 mM MgCl₂, 2 mM ZnCl₂.

Crystals were obtained in a micro-batch setup by mixing 0.5 µl volumes of 22.5 mg ml^{−1} hFBPase in 10 mM potassium/sodium phosphate pH 7.4, 2 mM MnCl₂, 5 mM MgCl₂, 2 mM ZnCl₂, 0.5 mM F-2,6-P₂ with reservoir solution consisting of 0.1 M Tris–HCl pH 8.5, 2 M ammonium sulfate. Crystals were cryoprotected and a data set was collected to a resolution of

Table 2

Systematic absences.

Type	$\langle I \rangle / \langle \sigma(I) \rangle$	No. of reflections
Screw axes		
0 <i>k</i> 0, <i>k</i> = 2 <i>n</i>	16.7	26
0 <i>k</i> 0, <i>k</i> = 2 <i>n</i> + 1	0.9	26
00 <i>l</i> , <i>l</i> = 4 <i>n</i>	12.2	31
00 <i>l</i> , <i>l</i> ≠ 4 <i>n</i>	1.1	94
<i>I</i> -centring		
<i>h</i> + <i>k</i> + <i>l</i> = 2 <i>n</i>	12.8	60612
<i>h</i> + <i>k</i> + <i>l</i> = 2 <i>n</i> + 1	10.5	60598
Pseudo-translation at (1/2, 1/2, 1/6)		
<i>h</i> + <i>k</i> + <i>l</i> /3 = 2 <i>n</i>	19.6	20386
<i>h</i> + <i>k</i> + <i>l</i> /3 = 2 <i>n</i> + 1	2.0	20406
Rest	9.7	80418
All	11.8	121210

2.2 Å (Table 1) from a cryocooled single crystal at 100 K on beamline PX-II at the Swiss Light Source using a wavelength of 0.979 Å and a MAR CCD detector of 165 mm diameter. Data were integrated and scaled using the *HKL* package (Otwinowski & Minor, 1997) and *SADABS* (Bruker), respectively. Indexing and integration was possible in primitive tetragonal, but not *I*-centred, settings, leading to unit-cell parameters of *a* = 121.5, *c* = 316.6 Å (Table 1). The likely presence of fourfold and twofold screw axes was established by analysis of the systematically absent reflections from data processed in space group *P422* (Table 2). As discussed in §2.3, the true space group is *P4*₁₂₁₂ and the presence of pseudo-translation (Fig. 2*a*) emulates *I*-centred symmetry. Assuming six FBPase molecules in the asymmetric unit, the Matthews coefficient (Matthews, 1968) is 2.8 Å³ Da^{−1} with a solvent content of 56%.

2.2. Data analysis

The data indexed readily and produced reasonable scaling statistics in a primitive 422 lattice (Table 1). To establish the space group, systematic absences were analyzed. While no reflections were measured along the *h* axis, analysis of the 0*k*0 reflections is consistent with the presence of a 2₁ screw axis. Likewise, the presence of only *l* = 4*n* reflections is consistent with both a 4₁ and a 4₃ screw axis, suggesting *P4*₁₂₁₂ or its enantiomorph as possible space groups (Table 2). Plots of the self-rotation function calculated with *XPREP* (Bruker) in space group *P422* are unremarkable, displaying the expected fourfold ($\kappa = 90^\circ$; not shown) and the mutually perpendicular arrangement of the fourfold and twofold axes in the $\kappa = 180^\circ$ section (Fig. 2*b*). Should noncrystallographic rotational symmetry be present, these axes would have to run parallel to a crystallographic axis. The *u* = 0 and *u* = 1/2 sections of the native Patterson map (Fig. 2*a*) contain three significant peaks of >20% of the origin signal at positions (*u*, *v*, *w*) = (1/2, 1/2, 1/6), (0, 0, 1/3) and (1/2, 1/2, 1/2). The presence of strong pseudo-translation manifests itself in a high value for the standard deviation of the mean normalized structure-factor amplitude *E*, $\langle |E^2 - 1| \rangle$, which is 1.152 but should be 0.736 for chiral space groups in the absence of twinning (Table 1), and also in the cumulative intensity distribution as reported by

TRUNCATE from *CCP4* (Winn *et al.*, 2011; Fig. 2c). If the special position at $(1/2, 1/2, 1/6)$ were crystallographic, no intensities would be measurable for a subset of reflections, while in the case of noncrystallographic symmetry certain reflections would be weak. Querying the structure-factor formula for reflection conditions that result in amplitudes $|F_{hkl}| = 0$ requires

$$\sum \exp[2\pi i(hx + ky + lz)] = -\sum \exp\{2\pi i[h(x + 1/2) + k(y + 1/2) + l(z + 1/6)]\}. \quad (1)$$

This leads to the condition $\exp[\pi i(h + k + l/3)] = -1$, which is fulfilled by 1/6 of all reflections in the data set that obey $h + k + l/3 = 2n + 1$, with n being an integer. While these $\sim 20\,000$ reflections are indeed weak, they are not absent, but have an $\langle I \rangle / \langle \sigma(I) \rangle$ value of 2.0 (Table 2). For comparison, the $h + k + l/3 = 2n$ reflections have correspondingly larger intensities of $\langle I \rangle / \langle \sigma(I) \rangle = 19.6$, while $\langle I \rangle / \langle \sigma(I) \rangle$ for the whole data set is 11.8 (Table 2). An equivalent reasoning for the

weaker Patterson peak at $(1/2, 1/2, 1/2)$ reveals only a slight decrease of 18% in the intensities of reflections $h + k + l = 2n + 1$ (Table 2) compared with the $h + k + l = 2n$ reflections, in line with the impossibility of indexing the data in an *I*-centred lattice where reflections $h + k + l = 2n + 1$ must be absent. Lastly, the vector $(0, 0, 1/3)$ will not change any reflection intensities. The source of the pseudo-translation and

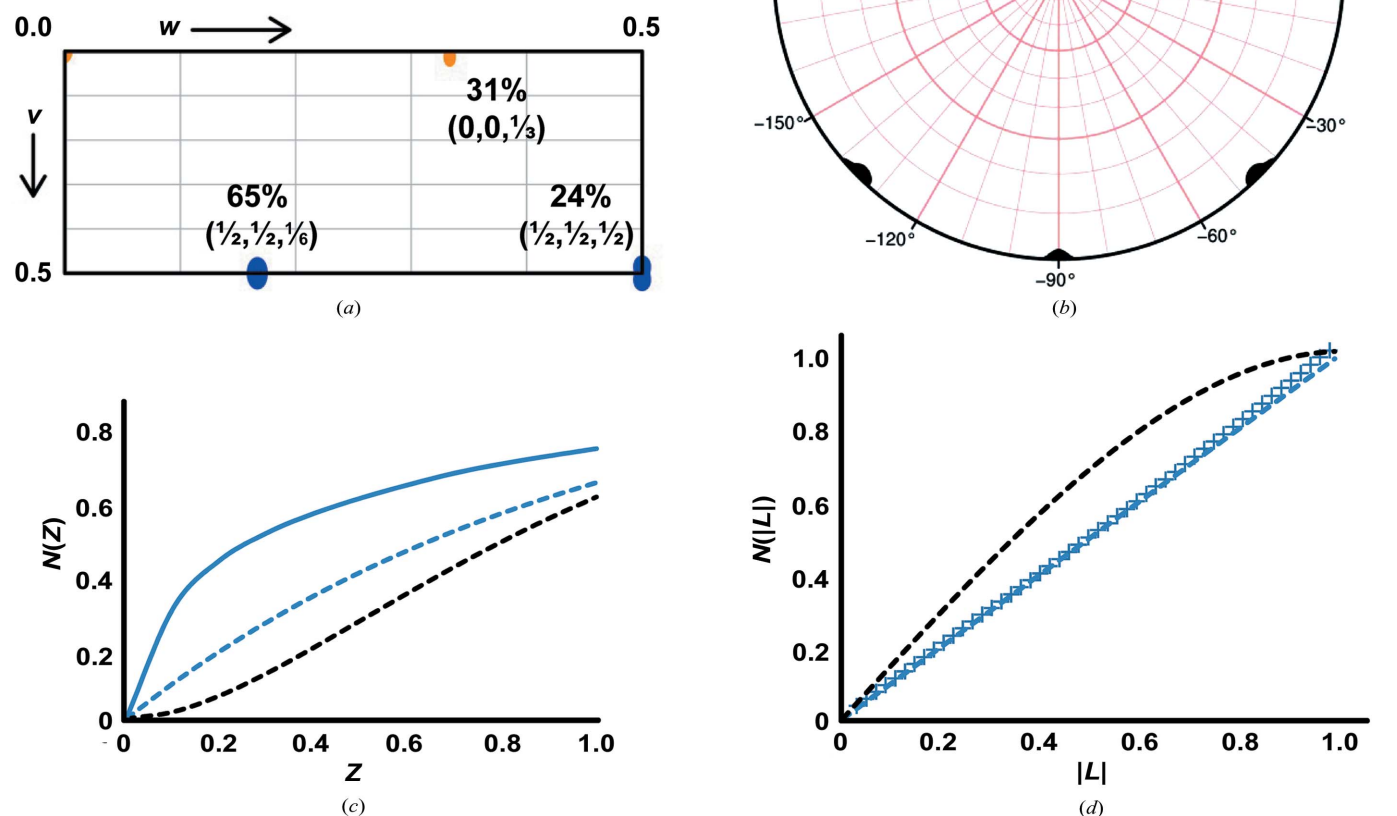


Figure 2

Detection of noncrystallographic symmetry in hIFBPase. (a) Superposition of the unique quarters of the $u = 0$ and $u = 1/2$ Patterson sections. The origin peak was removed and only peaks of $>10\sigma$ are displayed. The $u = 0$ section (orange) contains a single non-origin peak at fractional coordinates $(0, 0, 1/3)$ at a height of 31% of the origin peak. The peaks on the $u = 1/2$ (blue) section at fractional coordinates $(1/2, 1/2, 1/6)$ and $(1/2, 1/2, 1/2)$ have relative heights of 65 and 24%, respectively. Note that the peak at $(1/2, 1/2, 1/6)$ is the sum of the vectors $(1/2, 1/2, 1/2)$ and $(0, 0, 1/3)$. The Patterson function was calculated to 2.5 Å resolution using *XPREP* (Bruker). (b) Stereographic projection of the $\kappa = 180^\circ$ section of the self-rotation function. Peaks occur at the expected positions for 422 symmetry. (c) Cumulative intensity distribution $N(Z)$ of acentric reflections as a function of $Z = I/\langle I \rangle$. hIFBPase data are drawn as a continuous blue line. Dashed lines represent the theoretical distributions for perfectly twinned (black) and untwinned (blue) data. The shift to larger $N(Z)$ values indicates pseudo-translation, and possibly masks twinning. (d) *L*-test to detect the possible presence of twinning in the presence of pseudo-translation. The cumulative distributions and $N(|L|)$ of the intensities I are plotted as a function of $L = |I_1 - I_2|/(I_1 + I_2)$, where I_1 and I_2 are unrelated intensities (Padilla & Yeates, 2003). hIFBPase data are drawn as a continuous blue line, as in (c). Dashed lines are expected distributions for normal (blue) and perfectly twinned (black) data. The observed hIFBPase data show no strong deviations from the untwinned case. The mean value of $|L| = 0.48$ is close to that expected for un-twinned data (Table 1). The calculations in (c) and (d) were performed on data scaled in space group *P4*. Plots for data scaled in space group *P422* look virtually identical.

Table 3

Molecular-replacement and refinement statistics in different space groups.

Molecular replacement was performed with *Phaser* (McCoy *et al.*, 2007) using a dimer as the search model. Refinement was performed in *BUSTER* (Blanc *et al.*, 2004).

Space group	RF Z-score†	TF Z-score‡	Packing violations	LLG§	R/R _{free} (%)
<i>P4₁22</i>	57.9	97.3	0	27700	0.22/0.25
<i>P4₁2₁2</i>	57.9	114.5	0	32000	0.21/0.24
<i>P4₃22</i>	52.2	78.7	0	18400	0.25/0.28
<i>P4₃2₁2</i>	52.2	65.7	1	16800	0.24/0.28

† RF, rotation function. ‡ TF, translation function. § LLG, log-likelihood gain.

pseudo-centring only became clear after molecular replacement (discussed below). Owing to the presence of pseudo-translation and the corresponding strong correlation of some reflection intensities, global statistics that rely on the data following a Wilson distribution are skewed (Table 1). Thus, twinning tests based on the cumulative intensity distribution, the $|E^2 - 1|$ value (Fig. 2c) or moments on intensities or structure-factor amplitudes cannot be employed, and the pseudo-translation may mask the presence of twinning (Padilla & Yeates, 2003; Rudolph *et al.*, 2004; Zwart, Grosse-Kunstleve *et al.*, 2008; Read *et al.*, 2013). It is possible in principle that the hIFBPase data belong to Patterson symmetry *P4/m* with twinning emulating the higher metric symmetry *P4/mmm*. A twinning test based on local non-twin-related reflection pairs, the *L*-value (Padilla & Yeates, 2003), which is not influenced by the presence of pseudo-centring provided that suitable reflection pairs are chosen (Sliwiak *et al.*, 2015), shows little deviation from the expected values for untwinned data (Table 1, Fig. 2d), indicating that the hIFBPase data are not twinned. This turned out to be true after refinement (see below).

2.3. Phasing and refinement

Molecular replacement was performed to phase the hIFBPase data in the four space groups *P4₁22*, *P4₃22*, *P4₁2₁2* and *P4₃2₁2* using *Phaser* v.2.1.4 (McCoy *et al.*, 2007). FBPase is a homotetramer composed of a dimer of dimers. The C1/C2 dimer of an in-house FBPase structure was used as the search model. When tested separately, all space groups returned a single solution of three dimers with the same overall arrangement, whereby space group *P4₁2₁2* gave the strongest signal (Table 3). Of note, the latest version of *Phaser* will use the tNCS information present in the data to automatically select the correct space group. Refinement of all four solutions in *BUSTER* (Blanc *et al.*, 2004) using the same set of test reflections to calculate R_{free} indicated *P4₁2₁2* as the correct space group based on the lowest R_{free} value (Table 3). The model in space group *P4₁2₁2* was rebuilt in *Coot* (Emsley *et al.*, 2010) and refined using *BUSTER*. No NCS restraints were applied and each of the six protomers was defined as a TLS group. Loop 22–26 near the AMP-binding site and the catalytic loop 56–70 were not included in the model owing to a lack of electron density. Refinement statistics are collected in

Table 4

Refinement statistics in space group *P4₁2₁2*.

Values in parentheses are for the highest resolution shell.

PDB code	5ldz
Resolution range (Å)	39.8–2.2 (2.26–2.20)
No. of reflections	120699 (8818)
R_{cryst} †	0.206 (0.271)
R_{free} †	0.239 (0.286)
DPI‡ (Å)	0.24
Phase error§ (°)	31
R.m.s.d., bonds (Å)	0.012
R.m.s.d., angles (°)	1.66
Ramachandran plot¶ (%)	
Favoured	97
Allowed	3
Disallowed	0
<i>MolProbity</i> score††	1.24
Clashscore‡‡	1.33
No. of protein residues	1872
No. of sulfate ions	29
No. of Zn ²⁺ ions	9
No. of Cl ⁻ ions	2
No. of atoms	
Protein	14528
Ligands	154
H ₂ O	488
$\langle B \rangle$ (Å ²)	
Overall	46.6
Protein	46.2
Ligands	92.0
H ₂ O	43.3

† $R_{\text{cryst}} = \sum_{hkl} (|F_{\text{obs}}| - |F_{\text{calc}}|) / \sum_{hkl} |F_{\text{obs}}|$, where F_{obs} and F_{calc} are the structure-factor amplitudes from the data and the model, respectively. R_{free} is as R_{cryst} but calculated using a 5% test set of structure factors. ‡ Cruickshank diffraction-component precision index based on the *R* value (Blow, 2002). § The maximum-likelihood-based phase error was calculated with *PHENIX* (Zwart, Afonine *et al.*, 2008). ¶ Calculated using *PHENIX* (Zwart, Afonine *et al.*, 2008). †† The *MolProbity* score should approach the high-resolution limit (Chen *et al.*, 2010). ‡‡ Clashscore is defined as the number of unfavourable all-atom steric overlaps ≥ 0.4 Å per 1000 atoms (Word *et al.*, 1999).

Table 4. Coordinates and structure factors for hIFBPase have been deposited in the Protein Data Bank (PDB entry 5ldz). Analysis of electron-density maps calculated with anomalous differences and refined phases revealed significant peaks of $>5\sigma$ that could be either Zn²⁺ or Mn²⁺. At the wavelength of data collection (0.979 Å), the calculated values for zinc and manganese are $f''(\text{Zn}) = 2.5$ e and $f''(\text{Mn}) = 1.3$ e, pointing to zinc rather than manganese as the element present. As discussed in §3.4, owing to the 3.3-fold more frequent occurrence of trigonal bipyramidal coordination of zinc versus manganese in the Cambridge Structural Database (CSD) and previous FBPase crystal structures containing Zn²⁺ rather than Mn²⁺, the former ion was modelled at these positions (Fig. 8), although a mixture of Zn²⁺ and Mn²⁺ cannot be completely excluded.

3. Results and discussion

3.1. Combination of rNCS and tNCS in FBPase

The three dimers in the asymmetric unit of hIFBPase form one and a half FBPase tetramers, with the first tetramer composed of protomers *A*, *B*, *C* and *D*, and the second (*EFE'F'*) completed by crystal symmetry (Fig. 3a). Alignment of molecular symmetry axes with crystallographic elements is

quite common for FBPses from different organisms. 30 out of 90 structures in the PDB, including pig, rabbit and human FBPses, crystallized in five different space groups and contain only a single subunit in the asymmetric unit. The tetramer is constructed by crystallographic symmetry operations (Choe *et al.*, 1998, 2000; Weeks *et al.*, 1999; Choe, Iancu *et al.*, 2003; Choe, Nelson *et al.*, 2003; Iancu *et al.*, 2005; Shi *et al.*, 2013; Gao *et al.*, 2013; Barciszewski *et al.*, 2016). 50 more FBPses structures in three different space groups have a C1/C2 dimer in the asymmetric unit, and the tetramer is also completed by crystallographic symmetry. Others, such as pig FBPses in space group $P2_12_12_1$, contain a complete tetramer with the shortest molecular twofold axis almost aligned with the b axis (Ke, Liang *et al.*, 1991). The case of hFBPses is a combination of these examples. One complete tetramer is aligned parallel to the c axis. An additional C1/C2 dimer is also aligned with the c axis and completed to a tetramer by crystallographic symmetry (Fig. 3*a*).

Rearrangement of the three hFBPses C1/C2 dimers reveals a twofold rNCS axis located at fractional coordinates $(1/4, 1/4, z)$ with the dimers spaced by $1/3$ along z (Fig. 3*b*). This twofold axis runs parallel to the crystallographic fourfold, explaining the unremarkable self-rotation function (Fig. 2*b*). Since a twofold axis at $(1/4, 1/4, z)$ is equivalent to a symmetry operation $(-x + 1/2, -y + 1/2, z)$, combination of this NCS operator with those of the primitive tetragonal space groups of

Patterson symmetry $P4/mmm$ generates eight instances of a $(1/2, 1/2, 1/2)$ translation. The pseudo-body-centring introduced thereby leads to the observed Patterson vector at $(1/2, 1/2, 1/2)$. However, the height of this vector is only 24% of the origin peak (Fig. 2*a*), ruling out an I -centred lattice. Calculation of the native Patterson map at different high-resolution limits shows that this peak reaches 80% of the origin peak at 12 \AA , further showing that the I -centring is pseudo. The vector at $(1/2, 1/2, 1/2)$ combines with the pseudo-translation of $(0, 0, 1/3)$ along the NCS axis to form a strong signal at $(1/2, 1/2, 5/6)$, which is symmetry-related to $(1/2, 1/2, 1/6)$, thus explaining all of the peaks in the native Patterson map (Fig. 2*a*).

In the presence of tNCS, an additional twinning test is sometimes possible (Rudolph *et al.*, 2004). As a Patterson map of a twinned crystal contains the atomic distance information of both twin domains but no cross-peaks between them, a pseudo-translation vector in a merohedral twin should appear twice in the native Patterson map. The prerequisite is that the tNCS vectors are not superimposed by the twin operator. For diffraction data scaled in space group $P4$, the potential twin operator emulating pseudo- $P422$ symmetry $(k, h, -l)$ corresponds to a twofold rotational axis bisecting the ab plane. Unfortunately, since the pseudo-translation vector in hFBPses is parallel to the rNCS along the c axis, the twin operator would superimpose the tNCS vectors of the twin

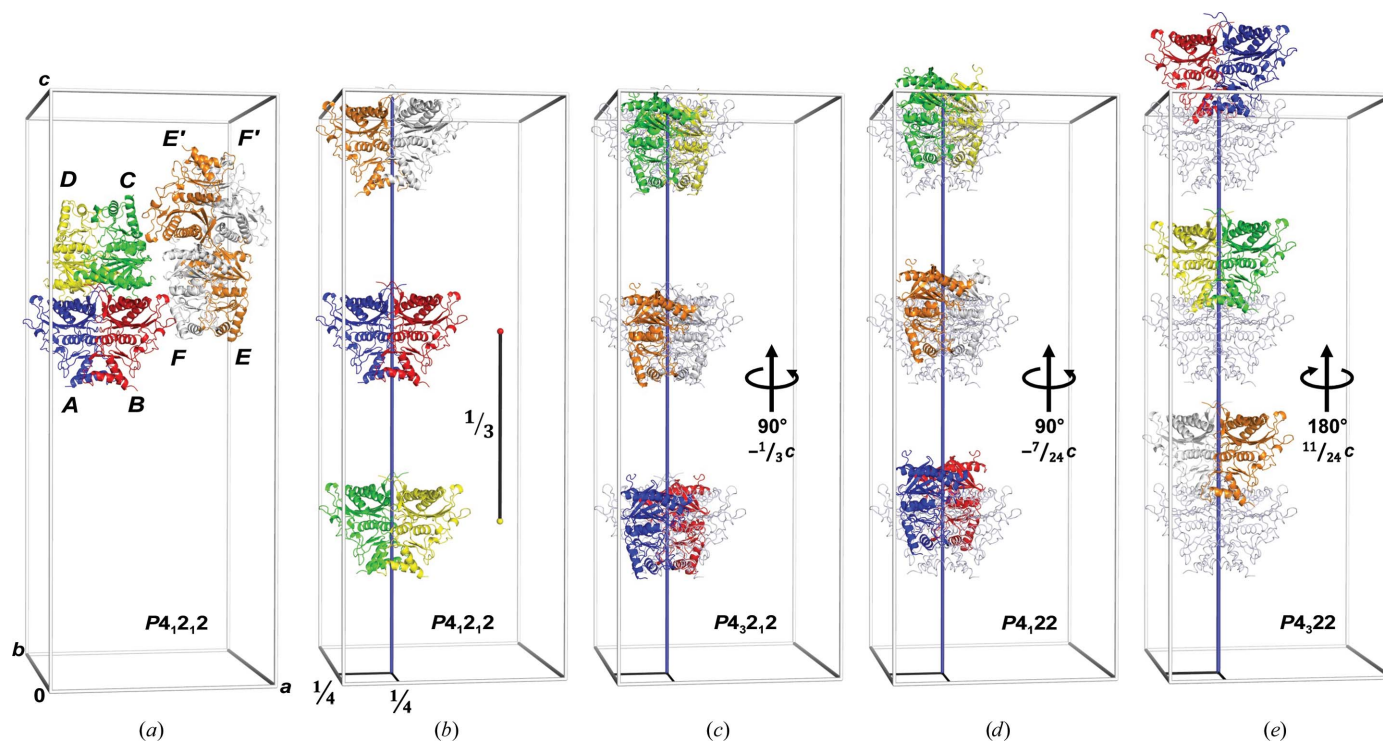


Figure 3

Molecular-replacement solutions for the hFBPses crystal. (a) The six protomers (A–F) in the asymmetric unit of space group $P4_12_12$, shown as differently coloured ribbons, form three dimers. Two of the C1/C2 dimers (AB and CD) associate to form a homotetramer, the biological unit of FBPses. The third dimer (EF) is complemented to form a tetramer by crystal symmetry ($E'F'$). (b) A different choice of the asymmetric unit visualizes a pseudo-translation vector (black bar) of fractional coordinates $(0, 0, 1/3)$, parallel to the c axis of the unit cell. The pseudo-translation vector relates dimers CD/AB , AB/EF and EF/CD . The dimers are placed along a twofold NCS axis at $(1/4, 1/4, z)$ that is drawn in blue. (c, d, e) Molecular-replacement solutions for space groups $P4_32_12$, $P4_122$ and $P4_322$ in the same colour code as in (a), with the $P4_12_12$ solution shown in grey as a reference. The search model was the $P4_12_12$ solution. The transformation from the solution in $P4_12_12$ to the other space group is given.

domains (with the inverse direction), thus not leading to any change in the native Patterson map. Therefore, the potential presence of twinning cannot be tested by analyzing the native Patterson maps in this particular case, and prior to refinement and judging the results based on R_{free} (see below), the L -test (Padilla & Yeates, 2003) was the sole statistic on which the absence of twinning in the hIFBPase data was based (Fig. 2c).

3.2. The same packing of hIFBPase in four space groups

Molecular replacement in the four space groups $P4_122$, $P4_322$, $P4_12_12$ and $P4_32_12$ each resulted in a single unique solution with a log-likelihood gain (LLG) of >16 000 (Table 3). The solution in $P4_12_12$ can be transformed into the $P4_32_12$ solution by a 90° clockwise rotation about $(1/4, 1/4, z)$ and a shift of $-1/3$ along z (Fig. 3c). The corresponding transformation into space group $P4_122$ is the same rotation but with a translation by $-7/24$ along z (Fig. 3d), and the transformation into space group $P4_322$ requires a 180° rotation about $(1/4, 1/4, z)$ and a shift of $11/24$ along z (Fig. 3e). Refinement of hIFBPase in the four space groups led to acceptable R_{free} values in all cases, although with a preference for space groups $P4_12_12$ and $P4_122$ (Table 3). The large cross-correlation coefficients between the phases in all four space groups of 0.81–0.84 confirm the notion that all solutions essentially describe the same situation. The question arises how packing in two enantiogenic space-group pairs is possible or, in other words, how the hIFBPase asymmetric unit can introduce a twofold axis and thereby generate additional fourfold screw axes of both hands (Fig. 3).

The handedness of the fourfold screw axis is a distinguishing feature of the enantiomorphic pairs $P4_12_12/P4_32_12$ and $P4_122/P4_322$. Thus, the arrangement of protomers in the asymmetric unit must enable both hands. Fig. 4 shows the molecular-replacement solution for $P4_12_12$ with the six individually coloured protomers simplified by the position of their centres of mass. Half of the molecules around a fourfold axis at $(1/2, 0, z)$ follow a left-handed ' $4_{1/3}$ ' axis, *i.e.* a fourfold screw axis with three complete turns along the unit cell: each molecule is shifted by $1/12$ with respect to its predecessor (Fig. 4a). A subset of molecules within this group follows a canonic 4_1 axis. Likewise, the other half of the molecules around the crystallographic fourfold screw axis also follow a left-handed ' $4_{1/3}$ ' axis, with a subset following a canonic 4_1 axis (Fig. 4b). Thus, both types of handedness are present in both subsets, explaining the

ambiguity along the fourfold axis. Similar considerations hold for the twofold or 2_1 axis parallel to the crystallographic a (and b) axis in the pairs $P4_12_12/P4_122$ and $P4_32_12/P4_322$. Accordingly, the four molecular-replacement solutions display virtually identical packing (Figs. 5a and 5b).

3.3. Requirements for and breakdown of the I -centring in hIFBPase

The presence of a twofold axis at $(1/4, 1/4, z)$ is a distinguishing feature of the $I4_122$ lattice compared with space groups with $P4/mmm$ Patterson symmetry. In hIFBPase, a twofold rNCS axis is present at this position that would in principle allow $I4_122$ as a higher symmetry space group. $I4_122$ is a minimal non-isomorphic supergroup for the four space groups $P4_122$, $P4_322$, $P4_12_12$ and $P4_32_12$, further corroborating why molecular replacement was possible in all of them. A 2_1 screw axis at $(1/4, 1/4, z)$ would generate an $I422$ lattice, but the corresponding primitive space groups would be $P422/P4_212$ or $P4_222/P4_212$, which are not supported by an analysis of systematic absences (Table 2), and which also did not deliver molecular-replacement solutions. Reflections with $l \neq 4n$ are absent, identifying a $4_1/4_3$ screw axis in the hIFBPase data, which leaves $I4_122$ as the sole option. A caveat for

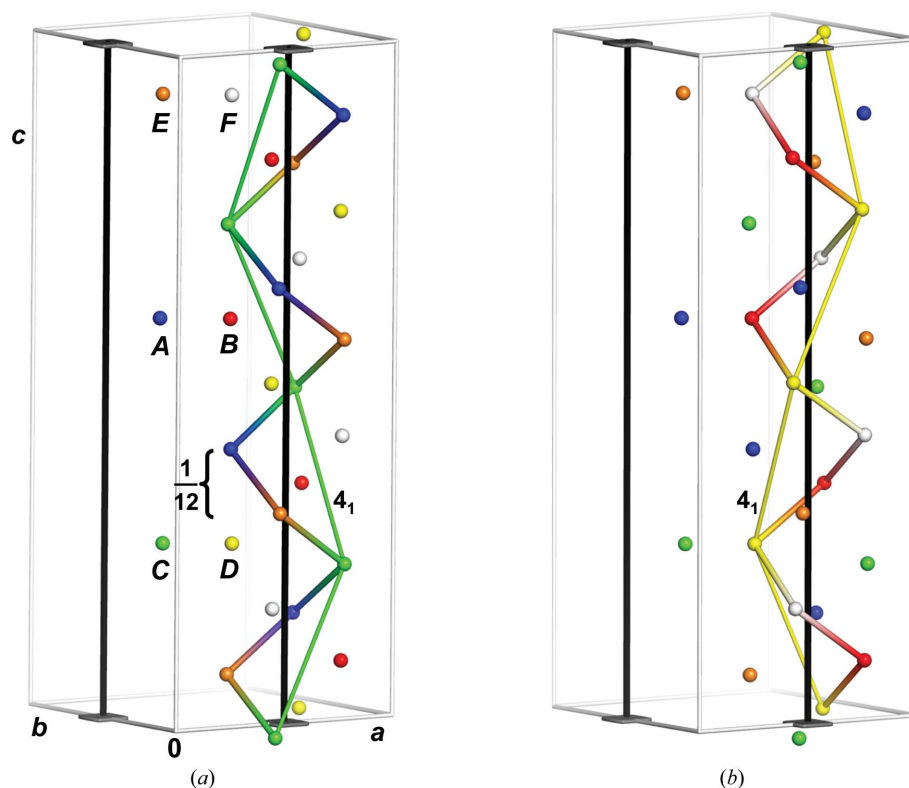


Figure 4
Space-group ambiguity owing to rNCS at $(1/4, 1/4, z)$. The six hIFBPase protomers are represented by spheres at the coordinates of the centre of mass. They are coloured individually and labelled A–F. (a) One half of the molecules related by the fourfold axis (black rod) forms a left-handed fourfold screw axis of three complete turns along the c axis. Successive molecules are translated by $c/12$. A subset of these molecules is related by a (right-handed) 4_1 axis (green) connecting symmetry mates. In fact, all like-coloured molecules are related by a 4_1 axis. (b) The other half of the molecules related by the fourfold axis also forms a left-handed helix, which incorporates a 4_1 axis (yellow), connecting two different symmetry mates in an alternating pattern.

Table 5

Geometric relations of the six protomers in the asymmetric unit.

Values in the upper triangle give the translation vectors in fractional coordinates. Note how close some of the translation components are to the rational numbers 1/2 or multiples of 1/3. The lower triangle of data denotes the r.m.s.d. values in Å after the superposition of all main-chain atoms. See Fig. 3(a) for the correspondence of the letters A–F to the protomers.

	A	B	C	D	E	F
A	—	0.507/0.514/0	0/−0.033/−0.331	0.505/0.483/−0.334	0.007/0.005/−0.668	0.514/0.517/−0.664
B	0.367	—	0.510/0.477/−0.334	0.002/−0.036/−0.331	0.513/0.522/−0.664	0.003/0.006/−0.668
C	0.370	0.182	—	0.508/0.473/−0.003	−0.002/0.016/−0.337	0.506/0.487/−0.333
D	0.208	0.353	0.378	—	0.508/0.487/−0.333	−0.009/0.022/−0.337
E	0.391	0.222	0.271	0.447	—	0.489/0.482/0.004
F	0.280	0.363	0.350	0.273	0.418	—

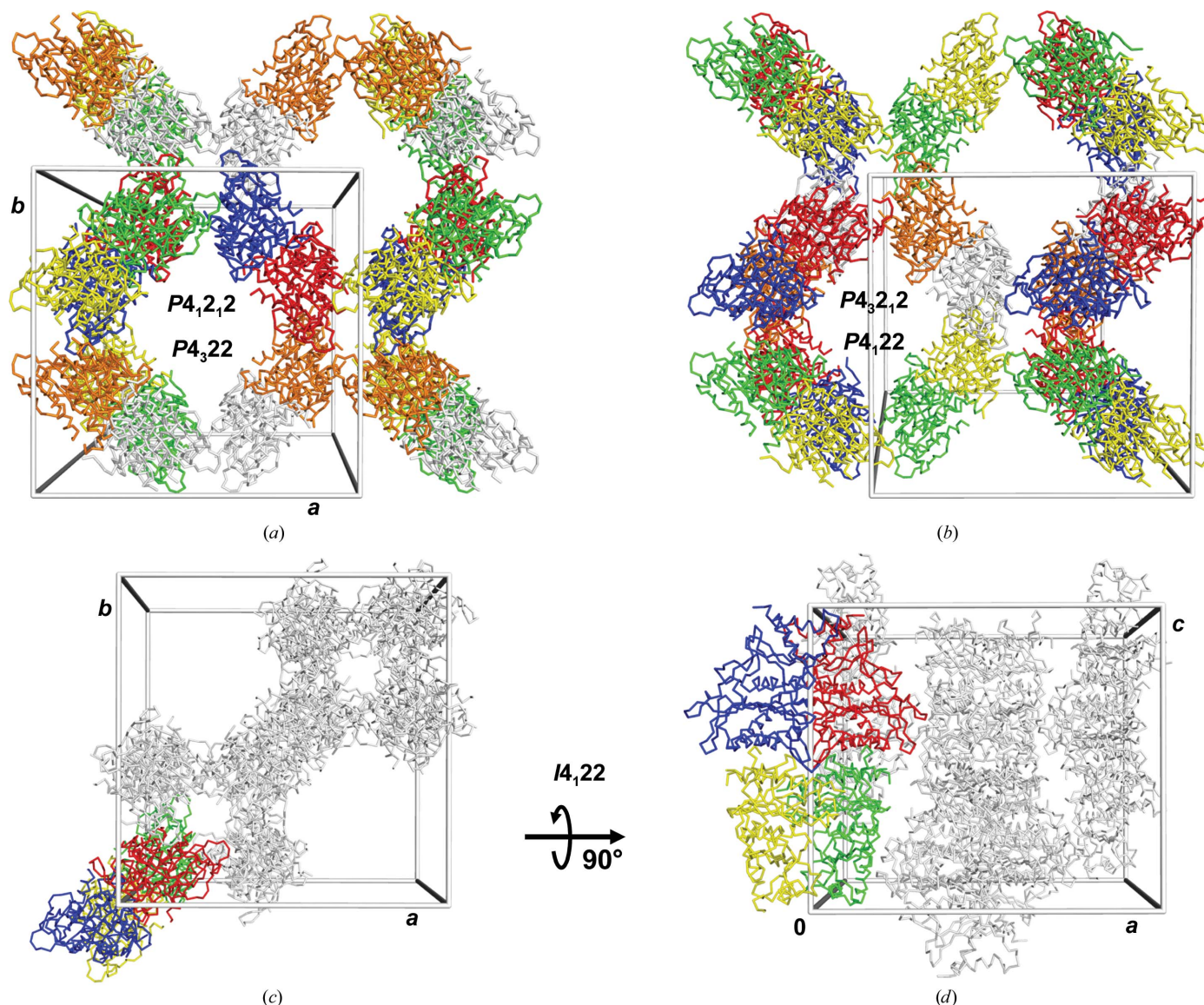


Figure 5

The same packing of hFBPase in tetragonal space groups. (a) Packing arrangement viewed along the *c* axis for the molecular-replacement solutions in space groups $P4_12_12$ and $P4_32_2$. (b) The same view for space groups $P4_32_12$ and $P4_12_2$. (c) Packing of the forced $I4_12_2$ setting with a *c*/3 axis and a crystallographic twofold instead of the observed rNCS. The default setting in the *I*-centred space group has the origin on the twofold axis along the *c* axis, leading to the shift compared with (a) and (b), but otherwise the packing is virtually identical. (d) A view rotated 90° compared with (c) shows a complete FBPase tetramer generated by crystal symmetry from the asymmetric unit, which in $I4_12_2$ would be a single subunit.

interpreting systematic absences is the possibility of pseudo-translation changing reflection intensities along the reciprocal axes, which might apply to hFBPase owing to the translational component of $\sim 1/3$ along the c axis. As mentioned above, the subset that is strongly altered by the vector $(1/2, 1/2, 1/6)$ is $(h + k + l/3)$, and $(0, 0, l)$ reflections with reflection condition

$l = 4n$ for 4_1 or 4_3 axes that are a part of this subset must have $l = 12n$. Because these reflections are even, they are not eliminated by the pseudo-translation but are slightly stronger [$\langle I \rangle / \langle \sigma(I) \rangle = 10$, $N = 11$]. An alternative approach is to calculate the reflection condition for absences owing to the $(0, 0, 1/3)$ vector for reflections along the l axis. The resulting

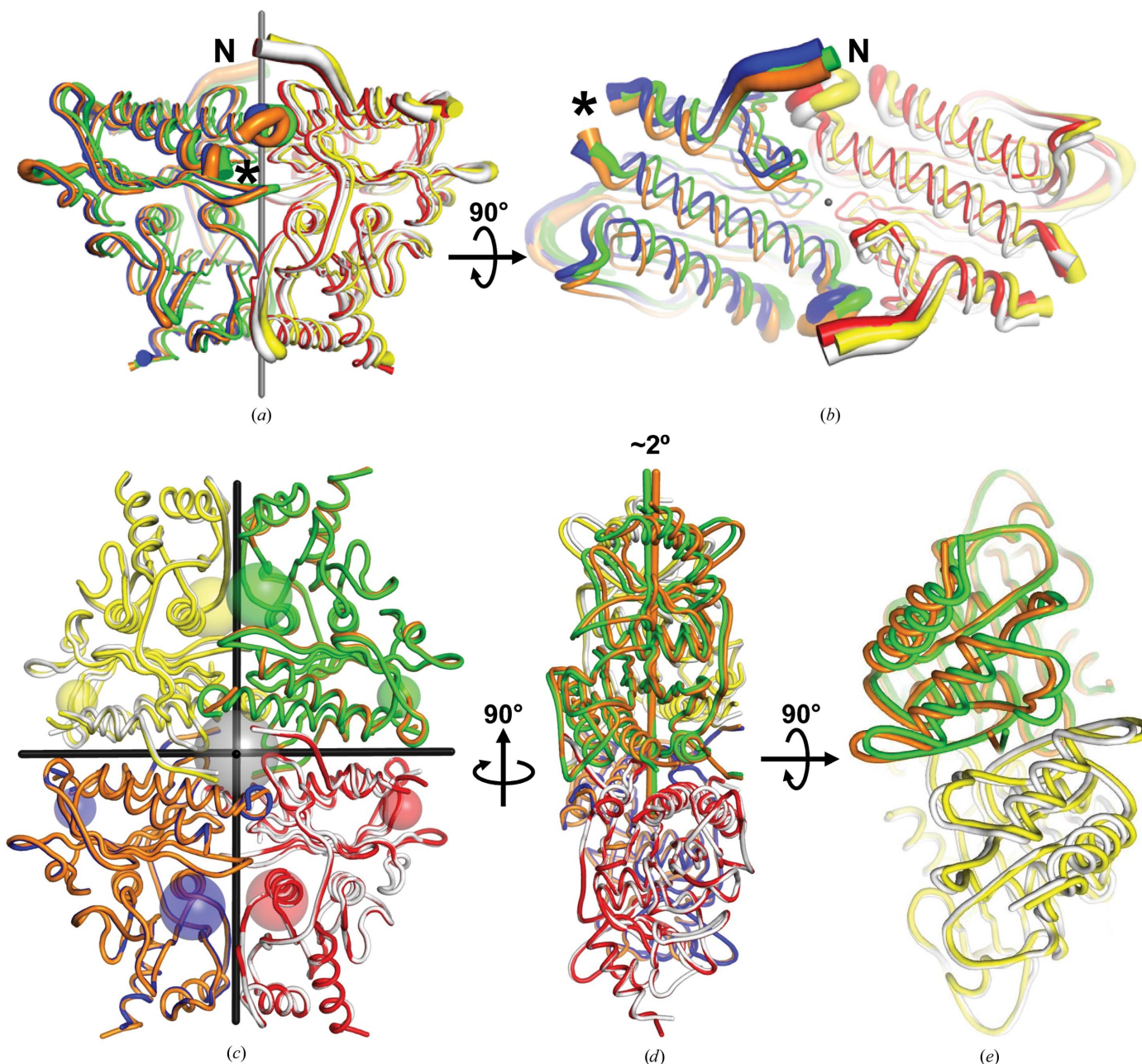


Figure 6 Structural variation of hFBPase protomers as the origin of pseudo-symmetry. (a) Side-on view of the FBPase dimers shifted along the rNCS axis shown in Fig. 3(b). The colour code also follows that in Fig. 3(b). The diameter of the backbone trace corresponds to the mean B value of this region, indicating possible flexibility at the N-terminus (labelled) and surface-loop regions. The asterisk denotes a missing loop region (residues 22–26). (b) View rotated 90° compared with that in (a), showing the lateral displacements of the dimers perpendicular to the rNCS axis in the ab plane. (c) Superposition of the two hFBPase tetramers onto one protomer (blue and orange) shows little differences in this orientation. The twofold axes of the almost D_2 -symmetric tetramers are marked in black. Important sites are shown as transparent spheres. Small spheres, allosteric AMP-binding sites; grey central sphere, second allosteric site; other large spheres, active and fructose 2,6-bisphosphate-binding sites. (d) A rotation by 90° compared with (c) reveals a tilted arrangement of dimers. The rotation axes for the upper dimers are drawn as rods, coloured according to one of the protomers, and differ in direction by 2.2° . (e) Top view along the rNCS axes shows displacements of the protomers in excess of 2 \AA .

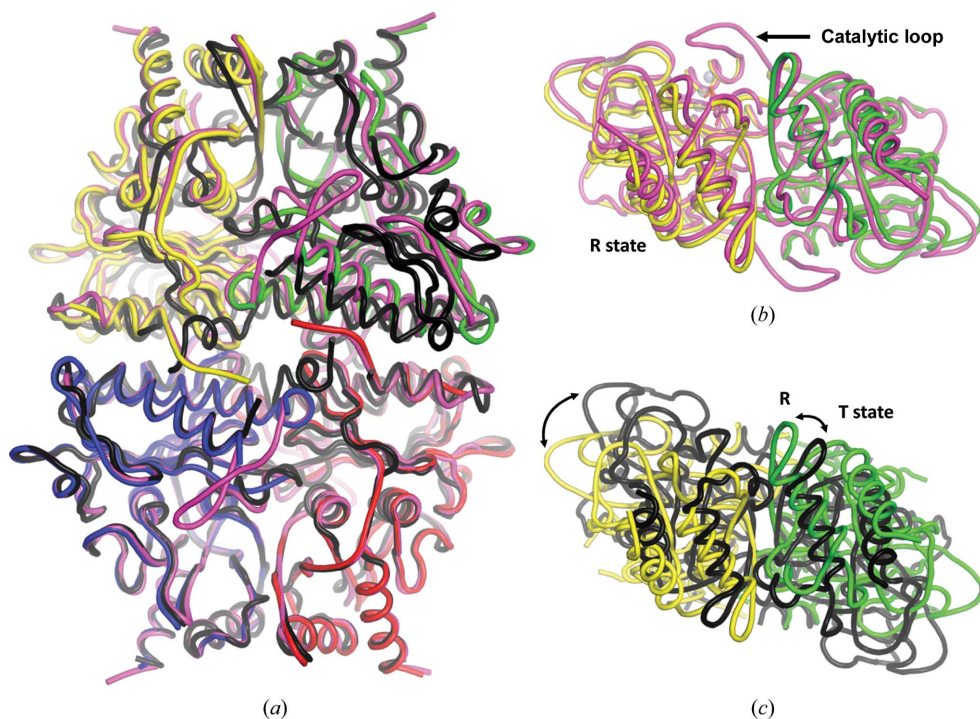


Figure 7
hIFBPase structure and comparison with related FBPsases in the R and T states. (a) Superposition of hIFBPase (subunits coloured yellow, green, red and blue) with R-state porcine liver FBPAse in complex with F6P (Choe *et al.*, 1998; magenta; PDB entry 1cnq) and with human liver FBPAse in the T state (Hebeisen *et al.*, 2011; black; PDB entry 2y5k). (b) View rotated 90° about the horizontal axis to show the close superposition of the R state of apo hIFBPase with the F6P-bound R state of porcine FBPAse. (c) The same view as in (b) but comparing the R state of hIFBPase (green/yellow) with the T state of hIFBPase (black). The two states differ by an $\sim 15^\circ$ rotation about the C1/C2 axis.

subset $(0, 0, 3n + 3/2)$ is impossible, *i.e.* this pseudo-translation vector does not alter any $(0, 0, l)$ reflection intensities. Taken together, the systematic absence analysis for the possible higher symmetry space group is unaffected by the pseudo-translation. Thus, if the rNCS at $(1/4, 1/4, z)$ were crystallographic, space group $I4_122$ would result. The question remains as to why hIFBPase does not form an I -centred lattice.

The two conditions that need to be fulfilled for I -centring are a crystallographic twofold at $(1/4, 1/4, z)$ and a pure translation of $(0, 0, 1/3)$. In a case where the translation were exactly $1/3$, the three copies of the hIFBPase dimer would be identical and the c^* axis would triple (the original c axis reduced to 105.5 Å). Space group $I4_122$ with a smaller c axis would harbour only a single protomer in the asymmetric unit, and crystal symmetry would construct an hIFBPase homotetramer with perfect 222 symmetry, similar to what has been observed with many other FBPAse structures (see above). Molecular replacement using data forcibly reduced in space group $I4_122$ with a $c/3$ axis resulted in a clear and single solution (Z -scores of 11.9 and 27.1 for the rotation and translation functions; overall LLG = 830) with the expected packing (Figs. 5c and 5d). However, this solution could not be refined to an R_{free} value of $<34\%$, further corroborating the primitive setting. Table 5 summarizes the geometric relations between the six protomers in the hIFBPase $P4_12_12$ asymmetric unit. The r.m.s.d. values between the protomers are of the order of 0.3 Å, mostly because of differences in the

conformation of the C-termini and the loop region 142–148. The rotation angles are close to either zero or 180° . Nine out of 15 possible twofold rotation combinations vary between 179.0 and 180.0° , with a mean of $179.6 \pm 0.3^\circ$. The remaining six cases have rotation components between 0.84 and 1.84° , with a mean of $1.21 \pm 0.47^\circ$. The translation components along the c axis are almost exactly $1/3$ or $2/3$ in all cases. By contrast, the translation vectors in the ab plane vary by as much as 4.6% (5.6 Å) from zero or $1/2$, indicating that the reason for the breakdown of symmetry, which prohibits an I -centred lattice, is owing to lateral translation of the hIFBPase dimers in the ab plane. A projection of the FBPAse dimers along the rNCS axis onto the ab plane confirms this hypothesis: lateral displacements from the rNCS axis are incompatible with this operator being crystallographic (Figs. 6a and 6b). In addition, while a superposition of the two

hIFBPase tetramers onto one protomer (blue and orange in Fig. 6c) shows little differences in the face-on orientation (Fig. 6c), a kinked arrangement of dimers is visible when the tetramers are viewed side-on (Fig. 6d) or from the top (Fig. 6e). The directions of the rotation axes for the upper dimers differ significantly by 2.2° , leading to displacements in excess of 2 Å, which is sufficient for the breakdown of body-centred symmetry.

3.4. Apo hIFBPase adopts the R state

The crystal structure of hIFBPase described here is the first example of the R state of the human liver isoform (Fig. 7). The rotation angle of the C1/C2 *versus* the C3/C4 dimers about the principal molecular axis is 2.9° , which is at the upper end of R-state angles of $1.3 \pm 0.9^\circ$ ($n = 36$, range 0 – 3.8°) found in porcine FBPAse crystal structures. A significant deviation from co-planarity (2.8 , 3.0 and 5.4°) of the subunits has also been observed for three human muscle FBPAse (hmFBPAse) structures (Shi *et al.*, 2013).

Binding of AMP to the allosteric sites induces a conformational change in FBPAse from its active R state to its inactive T state (Ke, Thorpe *et al.*, 1990; Choe *et al.*, 1998). In human liver FBPsases the average rotation angle of the T state is $14.5 \pm 0.4^\circ$ ($n = 15$, range 13.9 – 15.1°), which is very similar to that observed in porcine FBPAse T-state structures of 14.2 ± 1.2 ($n = 30$, range 10.5 – 17.1°). Three hmFBPAse structures

have similar rotation angles of $15.6 \pm 0.2^\circ$ (range 15.4–15.7°; Zarzycki *et al.*, 2011; Barciszewski *et al.*, 2016), which would

indicate that the amount of rotation in FBPases is generally of the order of 15°. This view has been challenged by a recent

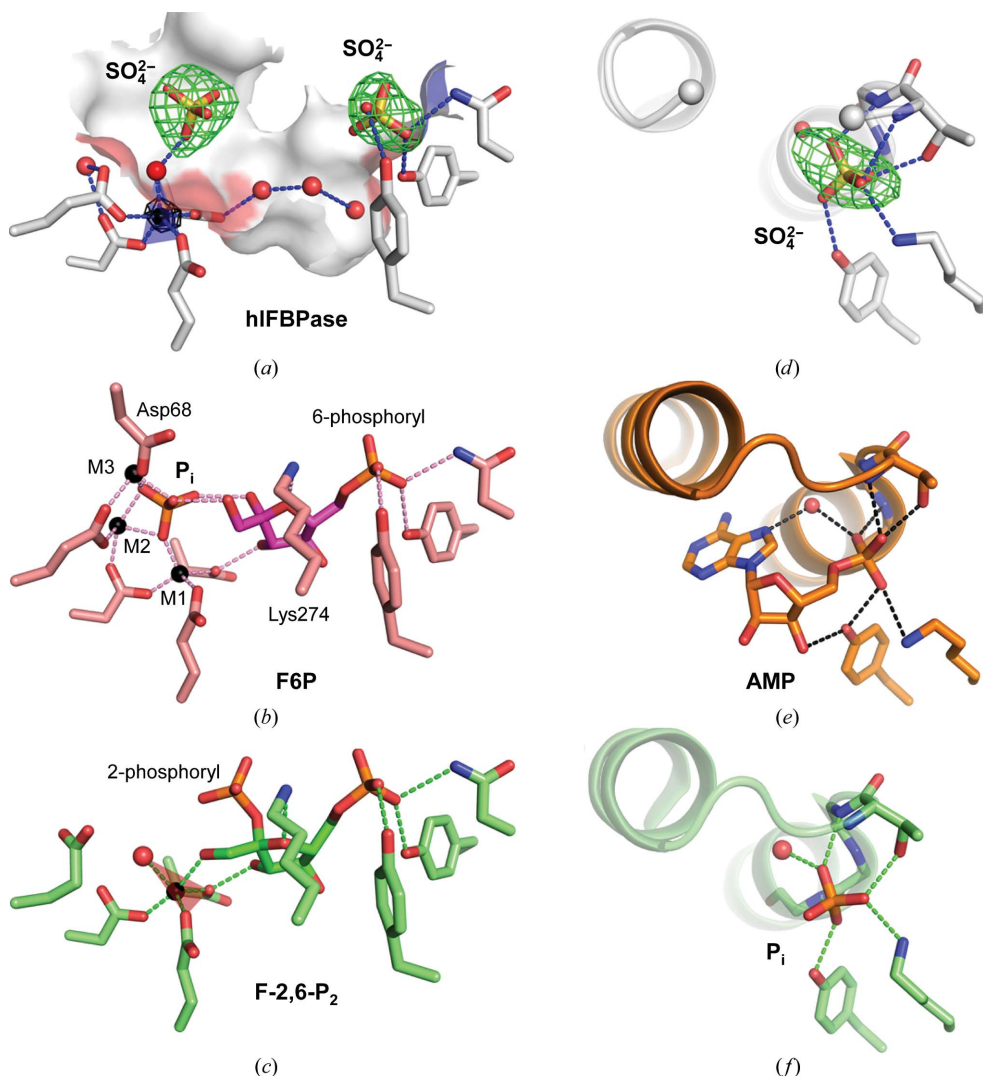


Figure 8

Comparison of the active and allosteric sites. (a) The active site in protomer *B* of hIFBPase is shown as a surface. The σ_A -weighted OMIT electron-density map contoured at 4 r.m.s.d. of the sulfate ions is drawn as a green mesh. The black mesh is a Fourier map using anomalous differences and refined phases as coefficients contoured at 7 r.m.s.d. The Zn^{2+} ion (black sphere) is coordinated by four acidic side chains and a water molecule in trigonal bipyramidal geometry. The transparent blue plane shows the base of the bipyramid. Possible hydrogen bonds ($<3.2 \text{ \AA}$) are shown as blue dashed lines. In the absence of a carbohydrate, a chain of water molecules (red spheres) fills the active site. (b) Active site of porcine FBPase in complex with F6P and phosphate (PDB entry 1cnq). The location of the sulfate ions in hIFBPase is close, but not identical, to the phosphates in this product complex. Three Zn^{2+} ions (small black spheres) were found in this structure. In general, the metal sites are denoted M1–M3. A notable difference from the hIFBPase structure is a Lys274 side chain that binds to the O4' atom of F6P but is flipped away in the apo state of hIFBPase. Asp68 is contributed from the catalytic loop, which has closed onto the active site of FBPase, but is disordered in hIFBPase. (c) Active site of porcine FBPase in complex with the competitive inhibitor F-2,6-P₂ (PDB entry 2qv). The 2'-phosphoryl group is located halfway between the positions of the inorganic phosphate in the product complex (b) and the sulfate ion in apo hIFBPase (a). The coordination of the Zn^{2+} ion is trigonal bipyramidal, but in a different arrangement compared with hIFBPase. The transparent blue plane shows the base of the bipyramid. (d) Allosteric AMP site in hIFBPase. A loop region is disordered and marked by grey spheres. The red mesh is the σ_A -weighted OMIT electron-density map contoured at 4 r.m.s.d. around the sulfate ion, which is bound to the phosphate-binding loop (P-loop) and the N-terminus of an α -helix. (e) The allosteric AMP site in porcine FBPase in complex with AMP. The loop that is missing in the hIFBPase structure is ordered in this complex. The sulfate ion in hIFBPase binds at the same position as the phosphoryl moiety of AMP. (f) Allosteric AMP site in porcine FBPase in complex with sulfate (PDB entry 2qv). The hydrogen-bonding pattern is the same as in hIFBPase shown in (d).

hmFBPase structure that showed a cruciform arrangement of the dimers, *i.e.* a rotation angle of close to 90° (Barciszewski *et al.*, 2016). Since the human muscle and liver FBPase isoforms share only 76.9% sequence identity (89.3% homology) over 337 residues and the muscle isoform has additional functions in the cell, including higher sensitivity of hmFBPase to AMP and its regulation by Ca^{2+} (Gizak *et al.*, 2012; Pirog *et al.*, 2014), some differences in their R/T transition behaviour might be expected. In solution, porcine FBPase subunits have been shown to exchange on a time scale of a few hours (Nelson *et al.*, 2001), indicating flexibility at the interfaces. Thus, the possibility that the rotation angle of FBPases might sometimes be influenced by crystal-packing effects cannot be discounted entirely.

Although excess F-2,6-P₂ was present during crystallization of hIFBPase to facilitate formation of the R state, the electron density does not support the presence of this competitive inhibitor in the active site. Instead, two sulfate ions from the crystallization medium are located in the active site (Fig. 8a). Comparison of hIFBPase with porcine FBPase in complex with F6P and phosphate (Choe *et al.*, 1998) and with porcine FBPase in complex with F-2,6-P₂ (Hines *et al.*, 2007) shows that the sulfate ions in hIFBPase are located near the positions of the phosphoryl groups in F6P and F-2,6-P₂ (Figs. 8b and 8c, respectively). The sulfate ion mimicking the 6-phosphoryl group is bound in the same manner in all structures by three hydrogen bonds from side chains of two tyrosines and an asparagine. The second sulfate ion in hIFBPase is located halfway between the positions of the inorganic phosphate in the

F6P/P_i complex (Fig. 8*b*; ~ 2.7 Å P–P distance) and the 2-phosphoryl group in the F-2,6-P₂ complex (Fig. 8*c*; ~ 2.2 Å P–P distance). While for steric reasons the 2'-phosphoryl group in F-2,6-P₂ cannot bind to the metal ion, in a total of 11 product complexes the inorganic phosphate is a direct ligand for either Zn²⁺ or Mg²⁺. By contrast, the corresponding sulfate ion in hFBPase is bound to the metal ion *via* a water molecule, a constellation that has not been observed before in FBPase crystal structures and may reflect a state during catalysis where inorganic phosphate is about to leave the active site after hydrolysis has completed.

Up to three metal ions have been observed in FBPase structures (termed M1–M3; Fig. 8*b*). The structure of hFBPase contains a single metal ion at position M1, which based on the crystallization conditions could in principle be Mg²⁺, Mn²⁺ or Zn²⁺. The M1 site in FBPase seems to be rather promiscuous: while Zn²⁺ was identified in the majority of structures, Mn²⁺, Mg²⁺ and Tl⁺ have also been located at this position. Based on strong OMIT electron density and an anomalous signal of >7 r.m.s.d. (Fig. 8*a*), Mg²⁺ could be excluded. Mn²⁺ appears to be less likely than Zn²⁺, since it has only half the anomalous signal at the data-collection wavelength (see §2). Also, refinement of hFBPase with Mn²⁺ at position M1 led to a smaller average *B* value for Mn²⁺ over the six molecules in the asymmetric unit compared with the metal-binding atoms (41 Å² versus 49 Å²), while refinement with Zn²⁺ yielded average values of 50 Å² for both sets of atoms. A distinction based on distances, which are similar for Zn²⁺ and Mn²⁺ (Harding *et al.*, 2010), was not possible at the resolution of hFBPase (2.2 Å). The coordination geometries observed in FBPase crystal structures at the M1 site include tetrahedral, octahedral and trigonal bipyramidal. In the majority of cases the M1 site is occupied by a tetrahedrally coordinated Zn²⁺, reflecting the preferred geometry of this ion. By contrast, the Zn²⁺ in hFBPase has trigonal bipyramidal coordination from four acidic side chains and a water molecule (Fig. 8*a*). A similar trigonal bipyramidal coordination of Zn²⁺, although tilted with respect to hFBPase, was observed in the crystal structure of porcine FBPase in complex with F-2,6-P₂ (Hines *et al.*, 2007; Fig. 8*c*). A search in the CSD for zinc- and manganese-containing compounds revealed only 103 small molecules with an Mn atom in trigonal bipyramidal geometry (0.57%), while a Zn atom in this geometry was present in 498 small-molecule crystal structures (1.87%), further hinting towards a Zn²⁺ at the M1 site. In conclusion, the M1 metal-binding site of FBPases is structurally versatile and can accommodate several cations in different coordination geometries. No metal ions are present at sites M2 and M3 in hFBPase. The metal ion at site M3 is coordinated by an aspartate side chain from the catalytic loop (Asp68 in Fig. 8*b*). Residues 55–70 of the catalytic loop are disordered in the hFBPase structure, possibly explaining the absence of the other cations.

The allosteric AMP site in hFBPase is also occupied by a sulfate ion, which mimics the position of the phosphoryl group of AMP (Fig. 8*d*). The anion is cradled in a classical P-loop followed by an α -helix. A conserved set of hydrogen bonds

from the side chain of a threonine and the NH groups of main-chain residues in the P-loop, together with the positive end of the helix dipole and a lysine side chain, neutralize the negative charges of the anion (Figs. 8*e* and 8*f*).

4. Conclusions

While a model for the T state of hFBPase is sufficient for structure-based drug-design purposes, the conformational picture of human liver FBPase has hitherto been incomplete. The structure of hFBPase in the R state fills this gap. It shows that the R state of hFBPase is similar to the R states of the rabbit, porcine and human muscle FBPases and that the human liver isoform engages in conformational changes similar in magnitude to those of porcine FBPase. The hFBPase structure exhibits a number of interesting properties, including a metal ion in a comparatively rare trigonal bipyramidal coordination bound *via* a water molecule to a sulfate ion that mimics the leaving inorganic phosphate after hydrolysis of the substrate. From a crystallographic point of view, the hFBPase structure is interesting for its peculiar arrangement of NCS elements, which emulate *I*-centred symmetry while the true symmetry is primitive with a *c* axis that is three times longer. A search in the PDB for structures with more than two molecules per asymmetric unit in the four space groups *P*₄₁₂₂, *P*₄₃₂₂, *P*₄₁₂₁ and *P*₄₃₂₁ that exhibit pseudo-translation returned 86 instances with a vector $>20\%$ of the Patterson origin peak. Of these, 33 emulate *I*-centring with a peak at (1/2, 1/2, *w*), but only three structures, PDB entries 4gqc, 2g6z and 3gfb, have *w* at rational fractions of the *c* axis (*w* = 1/2, *w* = 1/6 and *w* = 1/4, respectively). In none of these cases is the rNCS axis at a position to emulate crystallographic symmetry, so the case of hFBPase seems unique at present. However, given the high prevalence of pseudo-symmetry in macromolecular crystal structures of $\sim 8\%$ (Zwart, Grosse-Kunstleve *et al.*, 2008), similar cases are to be expected.

Acknowledgements

We thank Catherine Joseph for crystallization and the staff at SLS beamline PX II for support during synchrotron data collection. We are grateful to the *Phaser* developers that the hFBPase data could be used to improve the algorithms subsequent to structure determination and analysis of this case.

References

- Barciszewski, J., Wisniewski, J., Kolodziejczyk, R., Jaskolski, M., Rakus, D. & Dzugaj, A. (2016). *Acta Cryst.* **D72**, 536–550.
- Blanc, E., Roversi, P., Vonrhein, C., Flensburg, C., Lea, S. M. & Bricogne, G. (2004). *Acta Cryst.* **D60**, 2210–2221.
- Blow, D. M. (2002). *Acta Cryst.* **D58**, 792–797.
- Chen, V. B., Arendall, W. B., Headd, J. J., Keedy, D. A., Immormino, R. M., Kapral, G. J., Murray, L. W., Richardson, J. S. & Richardson, D. C. (2010). *Acta Cryst.* **D66**, 12–21.
- Choe, J. -Y., Fromm, H. J. & Honzatko, R. B. (2000). *Biochemistry*, **39**, 8565–8574.

- Choe, J.-Y., Iancu, C. V., Fromm, H. J. & Honzatko, R. B. (2003). *J. Biol. Chem.* **278**, 16015–16020.
- Choe, J.-Y., Nelson, S. W., Arienti, K. L., Axe, F. U., Collins, T. L., Jones, T. K., Kimmich, R. D., Newman, M. J., Norvell, K., Ripka, W. C., Romano, S. J., Short, K. M., Slee, D. H., Fromm, H. J. & Honzatko, R. B. (2003). *J. Biol. Chem.* **278**, 51176–51183.
- Choe, J.-Y., Poland, B. W., Fromm, H. J. & Honzatko, R. B. (1998). *Biochemistry*, **37**, 11441–11450.
- Dang, Q., Kasibhatla, S. R., Jiang, T., Fan, K., Liu, Y., Taplin, F., Schulz, W., Cashion, D. K., Reddy, K. R., van Poelje, P. D., Fujitaki, J. M., Potter, S. C. & Erion, M. D. (2008). *J. Med. Chem.* **51**, 4331–4339.
- Dang, Q., Kasibhatla, S. R., Reddy, K. R., Jiang, T., Reddy, M. R., Potter, S. C., Fujitaki, J. M., van Poelje, P. D., Huang, J., Lipscomb, W. N. & Erion, M. D. (2007). *J. Am. Chem. Soc.* **129**, 15491–15502.
- Dang, Q. *et al.* (2011). *J. Med. Chem.* **54**, 153–165.
- Diederichs, K. & Karplus, P. A. (1997). *Nature Struct. Biol.* **4**, 269–275.
- Emsley, P., Lohkamp, B., Scott, W. G. & Cowtan, K. (2010). *Acta Cryst. D* **66**, 486–501.
- Erion, M. D., Dang, Q., Reddy, M. R., Kasibhatla, S. R., Huang, J., Lipscomb, W. N. & van Poelje, P. D. (2007). *J. Am. Chem. Soc.* **129**, 15480–15490.
- Erion, M. D., van Poelje, P. D., Dang, Q., Kasibhatla, S. R., Potter, S. C., Reddy, M. R., Reddy, K. R., Jiang, T. & Lipscomb, W. N. (2005). *Proc. Natl Acad. Sci. USA*, **102**, 7970–7975.
- Gao, Y., Iancu, C. V., Mukind, S., Choe, J.-Y. & Honzatko, R. B. (2013). *Biochemistry*, **52**, 5206–5216.
- Geldern, T. W. von, Lai, C., Gum, R. J., Daly, M., Sun, C., Fry, E. H. & Abad-Zapatero, C. (2006). *Bioorg. Med. Chem. Lett.* **16**, 1811–1815.
- Gidh-Jain, M., Zhang, Y., van Poelje, P. D., Liang, J.-Y., Huang, S., Kim, J., Elliott, J. T., Erion, M. D., Pilkis, S. J., Raafat el-Maghrabi, M. & Lipscomb, W. N. (1994). *J. Biol. Chem.* **269**, 27732–27738.
- Gizak, A., Pirog, M. & Rakus, D. (2012). *FEBS Lett.* **586**, 13–19.
- Harding, M. M., Nowicki, M. W. & Walkinshaw, M. D. (2010). *Crystallogr. Rev.* **16**, 247–302.
- Hebeisen, P. *et al.* (2011). *Bioorg. Med. Chem. Lett.* **21**, 3237–3242.
- Hebeisen, P., Kuhn, B., Kohler, P., Gubler, M., Huber, W., Kitas, E., Schott, B., Benz, J., Joseph, C. & Ruf, A. (2008). *Bioorg. Med. Chem. Lett.* **18**, 4708–4712.
- Hines, J. K., Chen, X., Nix, J. C., Fromm, H. J. & Honzatko, R. B. (2007). *J. Biol. Chem.* **282**, 36121–36131.
- Iancu, C. V., Mukund, S., Fromm, H. J. & Honzatko, R. B. (2005). *J. Biol. Chem.* **280**, 19737–19745.
- Iversen, L. F., Brzozowski, M., Hastrup, S., Hubbard, R., Kastrop, J. S., Larsen, I. K., Naerum, L., Nørskov-Lauridsen, L., Rasmussen, P. B., Thim, L., Wiberg, F. C. & Lundgren, K. (1997). *Protein Sci.* **6**, 971–982.
- Karplus, P. A. & Diederichs, K. (2012). *Science*, **336**, 1030–1033.
- Ke, H., Liang, J. Y., Zhang, Y. & Lipscomb, W. N. (1991). *Biochemistry*, **30**, 4412–4420.
- Ke, H., Thorpe, C. M., Seaton, B. A., Lipscomb, W. N. & Marcus, F. (1990). *J. Mol. Biol.* **212**, 513–539.
- Ke, H., Thorpe, C. M., Seaton, B. A., Marcus, F. & Lipscomb, W. N. (1989). *Proc. Natl Acad. Sci. USA*, **86**, 1475–1479.
- Ke, H., Zhang, Y., Liang, J.-Y. & Lipscomb, W. N. (1991). *Proc. Natl Acad. Sci. USA*, **88**, 2989–2993.
- Ke, H., Zhang, Y. & Lipscomb, W. N. (1990). *Proc. Natl Acad. Sci. USA*, **87**, 5243–5247.
- Kitas, E. *et al.* (2010). *Bioorg. Med. Chem. Lett.* **20**, 594–599.
- Lai, C., Gum, R. J., Daly, M., Fry, E. H., Hutchins, C., Abad-Zapatero, C. & von Geldern, T. W. (2006). *Bioorg. Med. Chem. Lett.* **16**, 1807–1810.
- Matthews, B. W. (1968). *J. Mol. Biol.* **33**, 491–497.
- McCoy, A. J., Grosse-Kunstleve, R. W., Adams, P. D., Winn, M. D., Storoni, L. C. & Read, R. J. (2007). *J. Appl. Cryst.* **40**, 658–674.
- Nelson, S. W., Honzatko, R. B. & Fromm, H. J. (2001). *FEBS Lett.* **492**, 254–258.
- Otwinowski, Z. & Minor, W. (1997). *Methods Enzymol.* **276**, 307–326.
- Padilla, J. E. & Yeates, T. O. (2003). *Acta Cryst. D* **59**, 1124–1130.
- Pirog, M., Gizak, A. & Rakus, D. (2014). *Int. J. Biochem. Cell Biol.* **48**, 55–59.
- Read, R. J., Adams, P. D. & McCoy, A. J. (2013). *Acta Cryst. D* **69**, 176–183.
- Rudolph, M. G., Wingren, C., Crowley, M. P., Chien, Y. & Wilson, I. A. (2004). *Acta Cryst. D* **60**, 656–664.
- Shi, R., Chen, Z.-Y., Zhu, D.-W., Li, C., Shan, Y., Xu, G. & Lin, S.-X. (2013). *PLoS One*, **8**, e71242.
- Sliwiak, J., Dauter, Z., Kowiel, M., McCoy, A. J., Read, R. J. & Jaskolski, M. (2015). *Acta Cryst. D* **71**, 829–843.
- Tsukada, T., Takahashi, M., Takemoto, T., Kanno, O., Yamane, T., Kawamura, S. & Nishi, T. (2009). *Bioorg. Med. Chem. Lett.* **19**, 5909–5912.
- Tsukada, T., Takahashi, M., Takemoto, T., Kanno, O., Yamane, T., Kawamura, S. & Nishi, T. (2010). *Bioorg. Med. Chem. Lett.* **20**, 1004–1007.
- Visinoni, S., Khalid, N. F., Joannides, C. N., Shulkes, A., Yim, M., Whitehead, J., Tiganis, T., Lamont, B. J., Favalaro, J. M., Proietto, J., Andrikopoulos, S. & Fam, B. C. (2012). *Diabetes*, **61**, 1122–1132.
- Weeks, C. M., Roszak, A. W., Erman, M., Kaiser, R., Jörnvall, H. & Ghosh, D. (1999). *Acta Cryst. D* **55**, 93–102.
- Winn, M. D. *et al.* (2011). *Acta Cryst. D* **67**, 235–242.
- Word, J. M., Lovell, S. C., LaBean, T. H., Taylor, H. C., Zalis, M. E., Presley, B. K., Richardson, J. S. & Richardson, D. C. (1999). *J. Mol. Biol.* **285**, 1711–1733.
- Wright, S. W. *et al.* (2002). *J. Med. Chem.* **45**, 3865–3877.
- Wright, S. W., Carlo, A. A., Danley, D. E., Hageman, D. L., Karam, G. A., Mansour, M. N., McClure, L. D., Pandit, J., Schulte, G. K., Treadway, J. L., Wang, I.-K. & Bauer, P. H. (2003). *Bioorg. Med. Chem. Lett.* **13**, 2055–2058.
- Xue, Y., Huang, S., Liang, J.-Y., Zhang, Y. & Lipscomb, W. N. (1994). *Proc. Natl Acad. Sci. USA*, **91**, 12482–12486.
- Zarzycki, M., Kołodziejczyk, R., Maciaszczyk-Dziubinska, E., Wysocki, R., Jaskolski, M. & Dzugaj, A. (2011). *Acta Cryst. D* **67**, 1028–1034.
- Zwart, P. H., Afonine, P. V., Grosse-Kunstleve, R. W., Hung, L.-W., Ioerger, T. R., McCoy, A. J., McKee, E., Moriarty, N. W., Read, R. J., Sacchettini, J. C., Sauter, N. K., Storoni, L. C., Terwilliger, T. C. & Adams, P. D. (2008). *Methods Mol. Biol.* **426**, 419–435.
- Zwart, P. H., Grosse-Kunstleve, R. W., Lebedev, A. A., Murshudov, G. N. & Adams, P. D. (2008). *Acta Cryst. D* **64**, 99–107.